Center-to-limb variation of the solar oscillation

New results from MDI data

W. Schmidt, M. Stix, and H. Wöhl

Kiepenheuer-Institut für Sonnenphysik, Schöneckstrasse 6, D-79104 Freiburg, Germany (wolfgang, stix, hw@kis.uni-freiburg.de)

Abstract. Using 17 hours of full-disk MDI Doppler data we have investigated the center-to-limb variation of the oscillatory wave spectrum of the solar photosphere. Power distributions in the $k_h\nu$-plane are calculated for fields of $20° \times 20°$ on the Sun, centered at every $10°$ heliographic latitude. From the center-to-limb variation of the power in the f mode and the lowest 7 p modes we obtain information about the mean inclination of the oscillatory velocity vector with respect to the vertical direction. We find qualitative agreement with a model of adiabatic waves in an isothermal atmosphere, but generally the solar oscillations appear to be less inclined than the model oscillations. We find no indication for the existence of horizontal sound waves on the Sun.

Key words: Sun: oscillations

1. Introduction

At the solar surface p-mode oscillations are observed mainly as a vertical wave motion. This is a consequence of the refraction of acoustic waves towards the vertical direction; the diffraction occurs because the sound velocity decreases from the solar interior towards the surface. However, a horizontal velocity component generally must also exist, except for the spherically symmetric modes with degree $l = 0$. In particular the f mode, which essentially is a surface wave, should have horizontal and vertical velocity components of approximately the same magnitude.

Information about the horizontal velocity components can be obtained from the center-to-limb variation of the line-of-sight velocity measured via the Doppler effect. Stix & Wöhl (1974) used sequences of one-dimensional scans made at diverse positions on the solar disk. For each of these positions they computed the distribution of the power in the diagnostic diagram of wave number and frequency, and so could analyze the center-to-limb variation of the wave spectrum. The results confirmed the essentially vertical character of the solar oscillations.

The purpose of the present contribution is to improve the analysis of the horizontal and vertical oscillation components on the basis of the superior data now available from the SOHO spacecraft. The new data are two-dimensional on the solar surface and have much less noise than the one-dimensional ground-based data used in the earlier study. In addition, the field size and the duration are larger so that the resolution in the diagnostic diagram is much better (although we shall again consider limited fields at various disk positions so that the wave-number resolution is not given by the full disk but rather by the field size). With these data we are of course able to pay attention to the particular behavior of the specific modes of global oscillation, the f and p modes. This was not possible in the study of Stix & Wöhl (1974); at that time these modes had not yet been identified observationally, although a theoretical prediction (Ulrich 1970) had been made.

In Sects. 2–4 of this paper we describe the data treatment and the computation of the power spectra. The results are presented in Sect. 5; Sects. 6 and 7 contain a discussion of the geometric and atmospheric effects that influence the observed Doppler shift. This discussion is guided by a model of adiabatic oscillations of small amplitude in a plane-parallel isothermally stratified atmosphere.

2. The data

We used a sequence of solar oscillation measurements obtained with the Michelson Doppler Imager (MDI) on board of the Solar and Heliospheric Observatory (SOHO). The sequence lasted as long as MDI operated in the full-disk mode (see Scherrer et al. 1995) and consists of about 17 hours of MDI Dopplergrams taken every minute on June 10, 1996. Within these data there were only very few gaps; we reconstructed the missing data from values adjacent to those gaps. For the center-to-limb variation we selected areas on the Sun which at the beginning of the observing period were located on the solar meridian. The Sun was very quiet on the meridian on that day, but there was some strong activity in the western hemisphere (active region NOAA 7968, $2°$ N, $42°$ W).

The data arrays are 1024×1024 integer values of velocities, corrected for instrumental effects and calibrated to m/s. In these images the solar radius equals to 483 pixels. For the center of the solar disk the square pixel size corresponds to 1441.5×1441.5 km^2 on the Sun.

Send offprint requests to: W. Schmidt

3. Conversion of coordinates

It was our aim to follow physically the same areas on the Sun for the whole observing period of 17 hours. This is best possible with a selection of arrays that are equidistant in the heliographic coordinates. For the conversion of the x, y coordinates to heliographic coordinates in general the solar radius, the tilt P of the solar axis, and the latitude B_0 of the disk center are necessary. The solar axis tilt P had not to be taken into account, since this was compensated automatically on board of SOHO. For the solar equator position on the observing day $B_0 = 0.41°$, with a small increase of $0.005°$/h, was taken into account.

The velocity of the solar differential rotation was fitted for each hour to the formula

$$v_{\rm rot}/(\cos \Psi \sin \Phi) = A + B \sin^2 \Psi + C \sin^4 \Psi , \qquad (1)$$

where Ψ and Φ are the latitude and longitude (central meridian distance), respectively, and $v_{\rm rot}$, A, B, and C are velocities. The data of the array v are the measured velocity values averaged over one hour and selected for central meridian distance larger than $30°$. The constants A, B, and C are the fitted parameters of the differential rotation; their mean values for the whole period of investigation are 1790 m/s, -202 m/s, and -342 m/s, respectively.

It should be mentioned that the equatorial rotation velocity obtained here is about 10% smaller than the equatorial rotation velocity measured spectroscopically (e.g., Schröter 1985). To our knowledge no detailed discussion of this discrepancy exists in the literature. Scattered light from the disk center would indeed cause an apparent decrease of the rotational velocity. However, according to R.S. Bogart (1998, private communication) the effect of scattered light had been investigated and virtually ruled out as an explanation. Since the discrepancy is evidently caused by MDI, this problem should be investigated further. For the analysis below, the rotation velocity is unimportant, since we investigate small-scale oscillatory motions and a field-independent velocity offset would not affect the diagnostic diagrams. Only the compensation for the field displacement due to the rotation may be slightly incorrect. The variation of the line-of-sight component of the spacecraft velocity is only a few m/s per day and can be ruled out as an explanation for the measured rotation law.

Within each selected area the x and y coordinates of all pixels were transformed to heliographic coordinates, i.e., distance Φ from the central meridian and latitude Ψ. The longitude values were corrected for the rotational displacement since the beginning of the observation by means of Eq. (1). For computational reasons the coordinates were then multiplied by a factor 5; the result were 100×100 arrays with integer coordinate values, corresponding to fields of $20° \times 20°$ in heliographic coordinates. Within each subfield of $0.2° \times 0.2°$ all existing data were averaged. Near the solar limb an increasing amount of subfields appeared without any data. In these cases values were interpolated from adjacent subfields with data. With this procedure we constructed data sets of 100×100 spatial and 1000 temporal elements, corresponding to $20° \times 20° \times 1000$ min.

For the study of the center-to-limb variation we used a series of these 3D-arrays, centered at latitudes $0°$, $10°$, $20°$, ..., $80°$, and located along the meridian at the beginning ($t = 0$). Both hemispheres were analyzed independently.

In order to improve the sampling at intermediate latitudes, additional data sets at $45°$, $55°$, $65°$, and $75°$ (both North and South) were constructed and analyzed. Although these data sets did not contain independent information (due to the complete overlap with the data sets located at "even" latitudes), they were useful to verify the slope of the resulting curves.

4. Power spectra

The next step of the data analysis was the computation of power spectra, or "diagnostic diagrams", for each of the 3D-arrays. The Fourier transform of the time-dependent velocity signal is defined as

$$f(k_x, k_y, \omega) = \int_{-\infty}^{\infty} v_{\rm los}(x, y, t) e^{i(k_x x + k_y y + \omega t)} dx dy dt , \quad (2)$$

and is calculated as a discrete Fourier transform.

The power spectrum is

$$P(k_x, k_y, \omega) = f \times f^* . \qquad (3)$$

Since we have removed the solar rotation from the data, we can assume that the velocity signals do not have a preferred horizontal direction, and that, therefore, the power spectrum depends only on the horizontal wave number $k_h = (k_x^2 + k_y^2)^{1/2}$. The diagnostic diagrams are obtained by azimuthally averaging the power spectra in the (k_x, k_y)-plane. The size of the investigated fields is 243 Mm $\times$ 243 Mm on the Sun, about 1/3 of the solar radius, so the use of cartesian coordinates is justified.

From the total duration ($T = 60\,000$ s) and the horizontal dimension ($L = 243$ Mm) we have a frequency resolution of $\nu_0 = T^{-1} = 0.0167$ mHz and a wave number resolution of $k_0 = 2\pi/L = 0.026$ Mm^{-1}. (Note that we use the cycle frequency $\nu = \omega/2\pi$ instead of the angular frequency ω for the analysis of the observations. Consequently, the power spectra are indeed $k_h\nu$-diagrams.)

Fig. 1 shows the $k_h\nu$-diagram corresponding to disk center. About a dozen modes are visible. The lowermost ridge corresponds to global surface waves (the f mode) with the dispersion relation

$$\nu = \frac{1}{2\pi} \sqrt{g k_h} \qquad (4)$$

with $g = 274$ ms^{-2}. The dotted line in Fig. 1 marks the dispersion relation of the f mode. The horizontal wave number k_h is related to the degree l of the spherical surface harmonic by $k_h = (l(l + 1))^{1/2}/r_\odot$, with the solar radius $r_\odot = 696$ Mm. As an example of an off-center diagnostic diagram the power spectrum at $\theta = 55°$ is shown in Fig. 2. There is considerably less power at high frequencies than in Fig. 1, in particular for large k_h. Moreover, the noise level is higher in the off-center diagram.
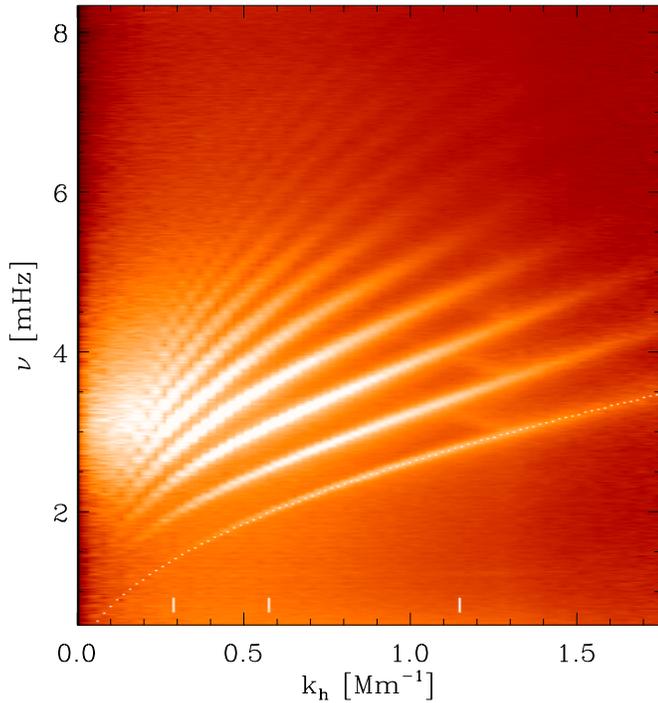
Fig. 1. The $k_h\nu$-diagram of the disk center, showing about a dozen modes. The intensity scale is logarithmic, as shown in Fig. 3. The dotted line is the dispersion relation of the f mode. The vertical bars indicate l-values of 200, 400, and 800, respectively

Fig. 2. The $k_h\nu$-diagram at $\theta = 55°$. Otherwise as Fig. 1

5. Center-to-limb variation

The projection procedure described above removes the fore-shortening effect of the observed area and creates arrays of equal size measured on the solar surface. The measured Doppler shifts have not been transformed, i.e. we analyze the power spectra of the line-of-sight velocity.

In order to calculate the mode power, we first determined a trial frequency of the eight lowest modes at an initial wave number, say $k_h = 0.75 \,\mathrm{Mm}^{-1}$.

In intervals containing 11 frequency points centered around each trial value we then calculated the precise location of the ridges from the Fourier transform of the ridge profile within the interval: for each ridge the phase angle of the first Fourier component defines the location of the ridge maximum. This procedure is fast and insensitive to noise. The computed ridge location was then used as trial value for the adjacent k_h positions both towards larger and smaller wave numbers. The precise locations of all ridges at disk center were then used as trial values for the power spectra of the data fields outside the disk center. Although we did not expect to find a significant variation of the ridge locations across the disk, we checked the ridge positions using the method described above. The velocity power was integrated along each ridge in two intervals of the horizontal wave number, namely $0.26 \le k_h \le 0.7 \,\mathrm{Mm}^{-1}$ and $0.7 \le k_h \le 1.3 \,\mathrm{Mm}^{-1}$, and in a frequency interval of 0.18 mHz, centered at the ridge maximum. Fig. 3 shows the frequency integration intervals for the wave number $k_h = 0.75 \,\mathrm{Mm}^{-1}$ (averaged over
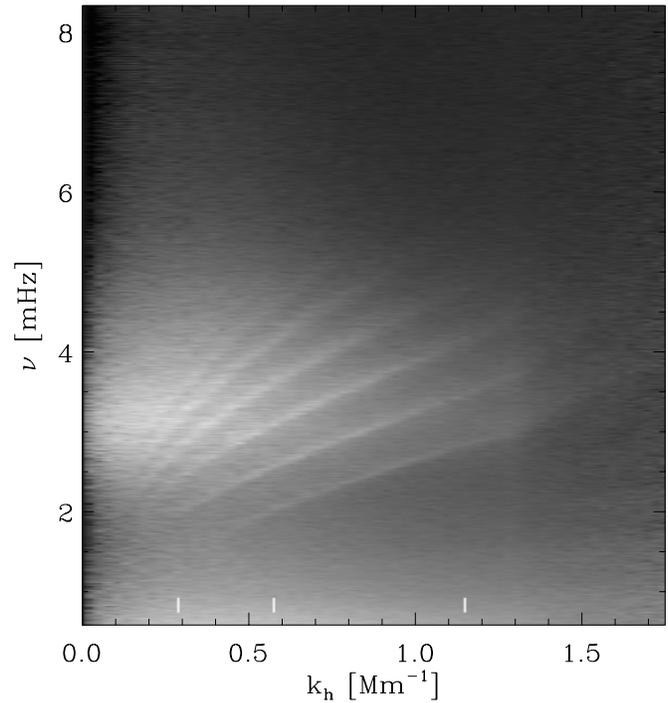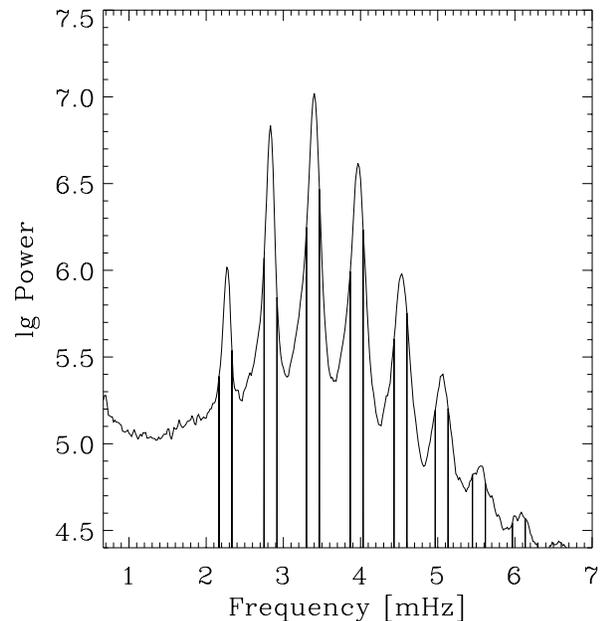

Fig. 3. Power spectrum at a wave number of $k_h = 0.75 \,\mathrm{Mm}^{-1}$ at disk center. The integration intervals of the ridges are indicated by vertical lines

two k_h points, i.e., over $\Delta k_h = 0.052 \,\mathrm{Mm}^{-1}$). We performed the same procedure also with a slightly wider interval, with no noticeable effect on the results, the additional power just shifts the curves vertically in Figs. 4a and 5a. Of course, foreshortening occurs near the limb. This effect permits full resolution of the wave number $1 \,\mathrm{Mm}^{-1}$ only down to $\cos\theta \approx 0.4$, and of wave number $0.5 \,\mathrm{Mm}^{-1}$ down to $\cos\theta \approx 0.2$. Figs. 4a and 5a
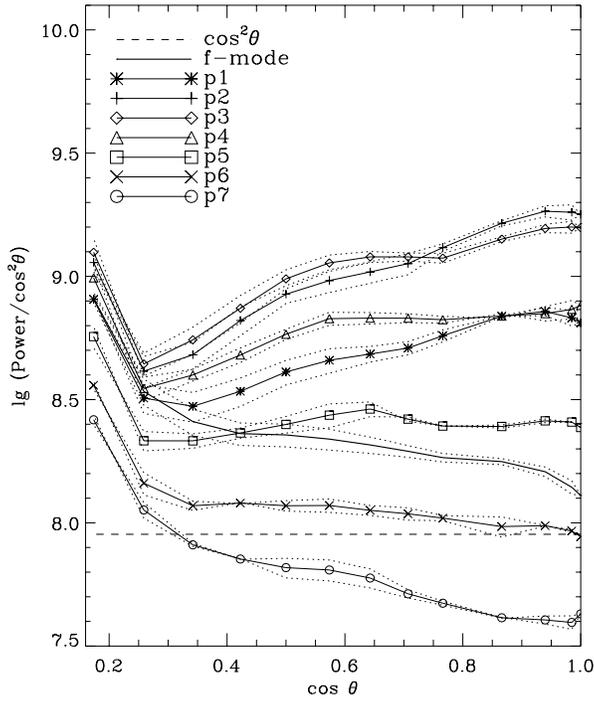
Fig. 4a. Center-to-limb variation of the power for the f mode and the lowest seven p modes for the low-k_h range ($k_h \leq 0.7\,\mathrm{Mm}^{-1}$). Dotted lines show results for North and South hemisphere of each mode.
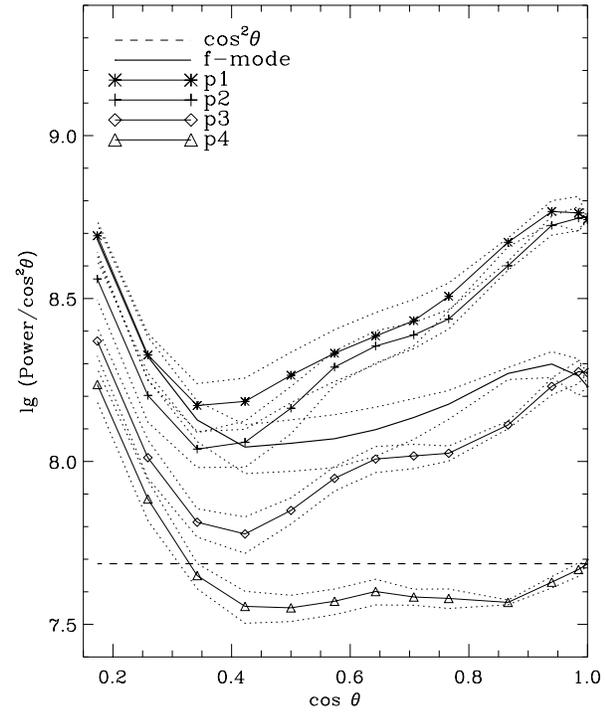

Fig. 5a. Center-to-limb variation of the power of the f mode and the lowest seven p modes, for the high-k_h range ($k_h \geq 0.7\,\mathrm{Mm}^{-1}$). Dotted lines show results for North and South hemisphere of each mode.
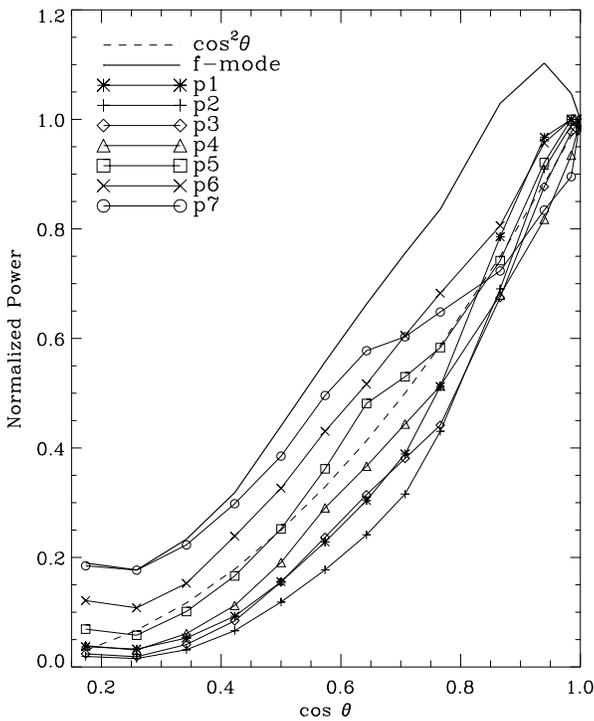

Fig. 4b. Same as Fig. 4a, but in a linear representation. Each curve is normalized to its value at disk center.
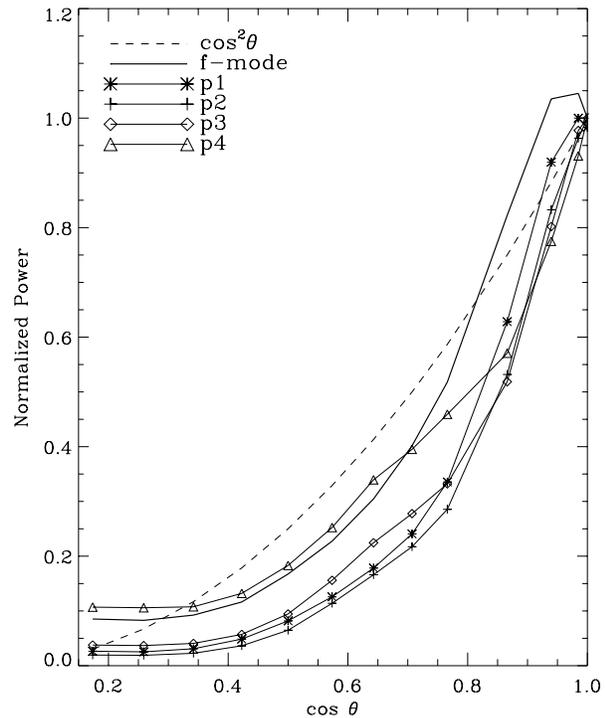

Fig. 5b. Same as Fig. 5a, but in a linear representation. Each curve is normalized to its value at disk center.

show a clear power increase below these $\cos\theta$ values; hence, from our point of view, this increase is mainly noise, divided by $\cos^2\theta$.

Fig. 4a displays the CLV of the power of the f mode and the lowest seven p modes for the low-k_h interval. The modes p_2 and p_3 have the largest power values. The horizontal line

corresponds to a vertical motion with constant v, cf. Eq. (8) below. The ordinate value for this curve is arbitrarily chosen. The variation of the f mode and of the modes p_4 to p_6 is rather close to such a horizontal line, whereas the power of the lower p modes decreases faster towards the limb. Fig. 4b shows the same results in a linear representation, with each curve normalized to its value at disk center. The increase of power very close to the limb should be treated with some caution: the ridges become very weak towards the limb (because of the decreasing line-of-sight component); in addition, the ridges are very close to each other at low wave numbers and some "crosstalk" may occur. Figs. 5a and 5b show the CLV of the mode power for the high wave number region. As compared to Fig. 4a, the mode p_4 is weaker in Fig. 5a by about one order of magnitude. The higher modes are still weaker, and are not included in Fig. 5 for this reason.

The northern and southern hemispheres have been analyzed independently with exactly the same procedure. Figs. 4 and 5 show North-South averaged curves; the results of each hemisphere are used as an estimate for the accuracy of the measurements (indicated by dotted lines around each mode), since there is no physical reason to expect a North-South asymmetry. There is, however, a moderate North-South difference of the f mode in the high-k_h range. This asymmetry includes the increase of the f-mode power at low latitude, which occurs only for the northern hemisphere (see Fig. 5). We have no explanation for this asymmetry.

6. Models

The interpretation of our results depends on the correct understanding of the projection effects of the solar surface velocity field. We address each of the data fields with a position angle, θ, which we assume constant within each field. In a local cartesian coordinate system the velocity vector $\mathbf{v}$ has the components (v_x, v_y, v_z). The z-axis coincides with the local surface normal, and the x-axis is in the plane defined by the z-axis and the line of sight. The z-axis is inclined with respect to the line of sight by the angle θ. If we introduce spherical coordinates with the inclination angle, γ, measured from the z-axis and the azimuth angle ϕ in the x, y-plane, with $\phi = 0$ in x-direction, the velocity components read

$$
\begin{aligned}
v_x &= v \sin\gamma \cos\phi , \\
v_y &= v \sin\gamma \sin\phi , \\
v_z &= v \cos\gamma .
\end{aligned}
\tag{5}
$$

The line-of-sight velocity v_{los} is then given by

$$
v_{\text{los}} = v(\sin\gamma \cos\phi \sin\theta + \cos\gamma \cos\theta) ,
\tag{6}
$$

The velocity power spectrum contains the time average of v_{los}^2:

$$
\begin{aligned}
\langle v_{\text{los}}{}^2 \rangle =\ & v^2\big(\langle \sin^2\gamma \cos^2\phi \rangle \sin^2\theta + \langle \cos^2\gamma \rangle \cos^2\theta \\
& + 2\langle \sin\gamma \cos\phi \sin\theta \cos\gamma \cos\theta \rangle \big) .
\end{aligned}
\tag{7}
$$

We assume that there is no correlation between the angles γ and ϕ, and that the power distribution in azimuth ϕ is isotropic.

In this case the last term of Eq. (7) makes no contribution; we obtain

$$
\langle v_{\text{los}}{}^2 \rangle = v^2 \left(\frac{1}{2} \langle \sin^2\gamma \rangle \sin^2\theta + \langle \cos^2\gamma \rangle \cos^2\theta \right) .
\tag{8}
$$

Thus, for purely vertical motion one would obtain a velocity power proportional to $\cos^2\theta$.

For the diverse wave modes in the solar atmosphere the angle γ can be determined from a theoretical model. The simplest model describes adiabatic waves of small amplitude in an isothermal plane-parallel atmosphere. In this case the variation with t and z is of the form

$$
\exp\left(i\omega t + \left(\frac{1}{2H} + ik_z \right) z \right) ,
\tag{9}
$$

where ω is the angular frequency, H is the pressure scale height, and k_z is the vertical wave number. In the present paper we do not solve the oscillation equations for the entire Sun, which would yield the frequencies ω as eigenvalues. Instead we consider ω as given, although we pay special attention to those values that are known as solar f- and p-mode frequencies. The vertical wave number is then given by the dispersion relation

$$
k_z^2 = \frac{\omega^2 - \omega_{\text{A}}^2}{c^2} + k_h^2 \left(\frac{N^2}{\omega^2} - 1 \right)
\tag{10}
$$

(e.g., Stix 1989). Here $\omega_{\text{A}} = c/2H$ is the acoustic cut-off frequency, $c = (\hat{\gamma} g H)^{1/2}$ is the adiabatic sound velocity, and $N = (\hat{\gamma} - 1)^{1/2} g/c$ is the Brunt-Väisälä frequency. For frequencies below the acoustic cut-off, which is for the greater part of the photospheric diagnostic diagram, we have $k_z^2 < 0$; we consider *evanescent* waves in an atmosphere of infinite extent, and therefore take the positive sign of $\Im(k_z)$. For frequencies above the cut-off k_z is real; in this case either sign of k_z yields the same result with Eq. (11) below. We eliminate the perturbations of pressure and density from the wave equations and obtain the ratio of the horizontal and vertical velocity components, $v_h = (v_x^2 + v_y^2)^{1/2}$ and v_z, and hence the angle γ:

$$
\tan^2\gamma = \frac{|v_h|^2}{|v_z|^2} = \frac{g^2 k_h^2 \, |i\hat{\gamma} H k_z + \hat{\gamma}/2 - 1|^2}{(\omega^2 - c^2 k_h^2)^2} .
\tag{11}
$$

In order to avoid confusion we denote the ratio of the specific heats by $\hat{\gamma}$ (we take $\hat{\gamma} = 5/3$).

We have calculated the inclination γ for the modes presented in the preceding section. The Ni I line at 676.8 nm is formed around the temperature minimum in the solar atmosphere, cf. Fig. 9 below, hence we take $T = 4400$ K in our model; for the mean molecular weight we take $\mu = 1.25$. With these specifications we have $H = 107$ km, $c = 7.0$ km/s, $\omega_{\text{A}} = 0.0327\,\text{s}^{-1}$, and $N = 0.0320\,\text{s}^{-1}$.

The dispersion relation for the f mode is $\omega_{\text{f}}^2 = g k_h$. Hence expression (10) for the vertical wave number can be simplified:

$$
\begin{aligned}
k_z^2 &= \frac{k_h}{\hat{\gamma} H} - \frac{1}{4H^2} + k_h^2 \left(\frac{\hat{\gamma} - 1}{\hat{\gamma} H k_h} - 1 \right) \\
&= -\left(\frac{1}{2H} - k_h \right)^2 ,
\end{aligned}
\tag{12}
$$

Table 1. Inclination γ of the wave vector with respect to the local vertical direction, for adiabatic waves in an isothermal atmosphere

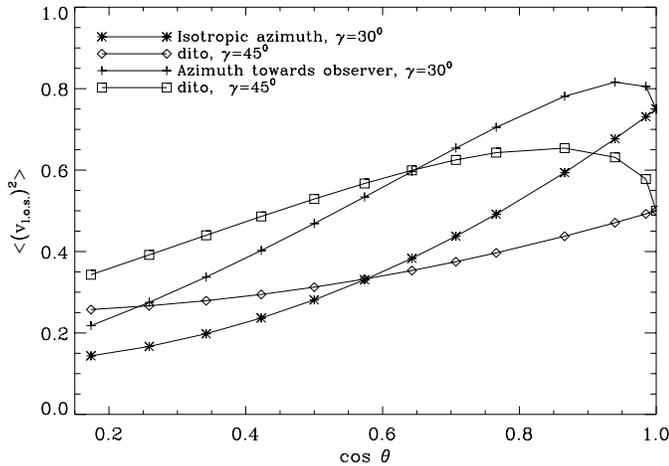| Mode	$k_h = 0.5\,\mathrm{Mm}^{-1}$	$k_h = 1.0\,\mathrm{Mm}^{-1}$
f	$45°$	$45°$
p_1	$30°$	$30°$
p_2	$20°$	$20°$
p_3	$13°$	$12°$
p_4	$10°$	$4°$
p_5	$6°$	$5°$
p_6	$4°$	$6°$
p_7	$2°$	$7°$

Fig. 6. Calculated center-to-limb variation of $\langle (v_{\mathrm{los}}^2 \rangle$ for inclination angles $\gamma = 45°$ and $\gamma = 30°$, for isotropic and non-isotropic distributions of azimuth angles ϕ

and $k_z = \pm i(1/2H - k_h)$. With the scale height as specified, we have $2 k_h H < 1$ in the range of horizontal wave numbers considered here, and therefore take the upper sign of k_z. Eq. (11) then yields

$$\tan^2 \gamma = \frac{|\hat{\gamma}(Hk_h - 1/2) + \hat{\gamma}/2 - 1|^2}{(1 - \hat{\gamma}Hk_h)^2} = 1 \,. \qquad (13)$$

That is, the angle γ is exactly $45°$ for the f mode, independently of the horizontal wave number.

The angles γ listed in Table 1 are calculated for the central horizontal wave numbers of the two k_h-ranges; within each of these ranges there is only a very small variation of γ. With increasing p-mode number γ decreases; at high frequency, in particular at and above the acoustic cut-off near 5 mHz, the wave vector becomes almost vertical. A minimum occurs near the cutoff itself, which is approximately at p_7 for $k_h = 0.5$ Mm^{-1}, and at p_4 for $k_h = 1\,\mathrm{Mm}^{-1}$. At a given frequency γ increases with increasing horizontal wave number k_h.

Let v^2 be the squared Fourier amplitude for a pair (k_h, ν). For this pair, and for the corresponding angle γ calculated with (11), we may then calculate the line-of-sight power $\langle v_{\mathrm{los}}^2 \rangle$ according to Eq. (8), as a function of θ. For all values γ of interest in the present context this function is monotonously decreas-
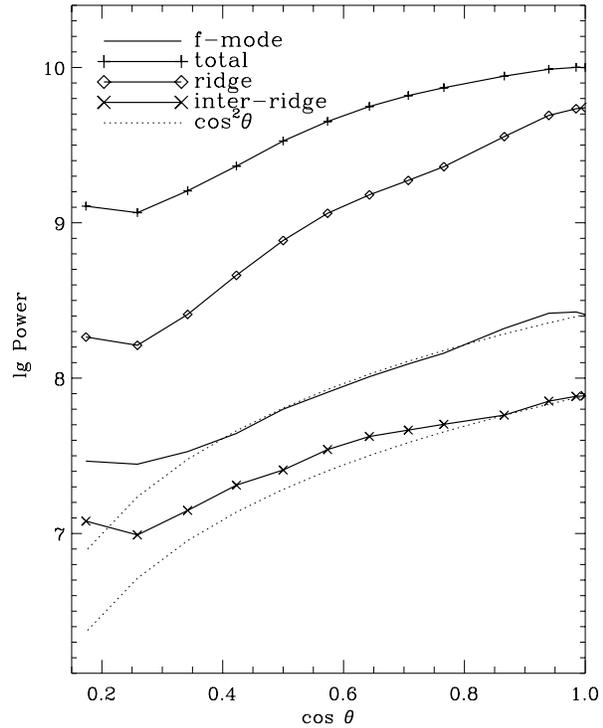

Fig. 7. Center-to-limb variation of the total power, ridge power, and f-mode power, in comparison to the curve $F(\cos\theta) = \cos^2\theta$, and the inter-ridge power measured close to the f-mode.

ing as θ increases. Two examples which, according to Table 1, represent the modes f and p_1, are shown in Fig. 6.

A maximum such as found for the modes f and p_1 around $\cos\theta = 0.9$ (Figs. 4b and 5b) cannot be explained in this way. However, if we allow for an anisotropy in the azimuthal distribution and calculate $\langle v_{\mathrm{los}}^2 \rangle$ according to Eq. (7), such a maximum is possible, as also illustrated in Fig. 6 for two values of the inclination γ and an azimuthal distribution that distinguishes the direction towards the observer.

In order to compare the center-to-limb variation of the modes with the global behavior of the velocity power in our data we have integrated the total power and the power of the f mode and the seven lowest p modes in the range $0.26 \le k_h \le 1.04\,\mathrm{Mm}^{-1}$ and $0.66 \le \nu \le 6.6$ mHz. Fig. 7 displays the result for the total power, the power contained in the eight ridges, and the f-mode power as a function of $\cos\theta$. The f-mode power deviates from the $\cos^2\theta$ curve only for values of $\cos\theta$ below 0.4., whereas the total p-mode power decreases faster towards the limb. The inter-ridge power was measured exactly in the same way as the mode power, in a 0.18 mHz wide frequency band below the f-mode.

7. Dependence on height in the atmosphere

The center-to-limb measurements mix two different types of information: (i) the variation of the vertical and horizontal velocity components, v_z and v_h, due to the projection effect, and (ii) the increasing height for observations off disk center due to
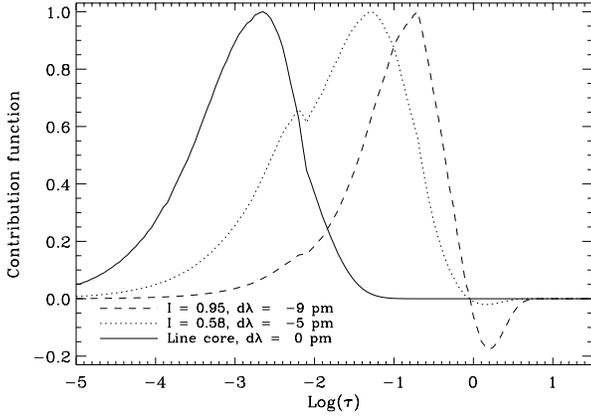
Fig. 8. Photospheric line-depression contribution function of the Ni I line at 676.8 nm, for the line core and for ± 5 and ± 9 pm from the line center

the inclined line of sight which moves the optical depth, where the line core is formed, outwards. This opacity effect depends on the spectral line used for the velocity measurements. The MDI velocity data are measured with the Ni I line at 676.8 nm. We have calculated the photospheric line-depression contribution function of this line as described by Grossmann-Doerth (1994). The three curves correspond to line center, line wing at half maximum and far wing at an intensity of 95% of the adjacent continuum. The contribution function is rather broad, which makes the line rather insensitive to an inclination of the line of sight. MDI uses a range of ± 15 pm centered around the line core for the Doppler measurements (Scherrer et al. 1995), so the velocity measurements are height-averaged over a significant range of optical depths.

The projection effects and the effects of non-vertical motion can be described by the simple geometrical model outlined above, in combination with the theoretical model of adiabatic waves in an isothermal atmosphere. For a first discussion it may suffice to assume that the optical depth varies in proportion to $\cos \theta$. The range $\cos \theta = 1 \ldots 0.2$ then corresponds to a height range of ≈ 100 km; to be specific, we take the 115-km range from $\tau = 0.001$ to $\tau = 0.0002$ in model C of Vernazza et al. (1981). We interpolate this range for the values Δz in steps of $\Delta \cos \theta = 0.1$. With these values, and for a given mode and given horizontal wave number, we then determine the vertical wave number and the angle γ according to (10) and (11), and finally the line-of-sight power according to (8). The factor v^2 in that equation is

$$v^2 = \exp\left(\Delta z(\theta)\left(\frac{1}{H} - 2\Im(k_z)\right)\right) . \tag{14}$$

This factor comprises the amplitude increase that is due to the decrease of the density, and the amplitude decrease that is due to the evanescent character of the waves. In all cases considered here the net effect is $v^2 \geq 1$; this factor alone would therefore cause an increase of the mode power with decreasing $\cos \theta$, in particular for the high frequencies above the acoustic cut-off where $\Im(k_z) = 0$.
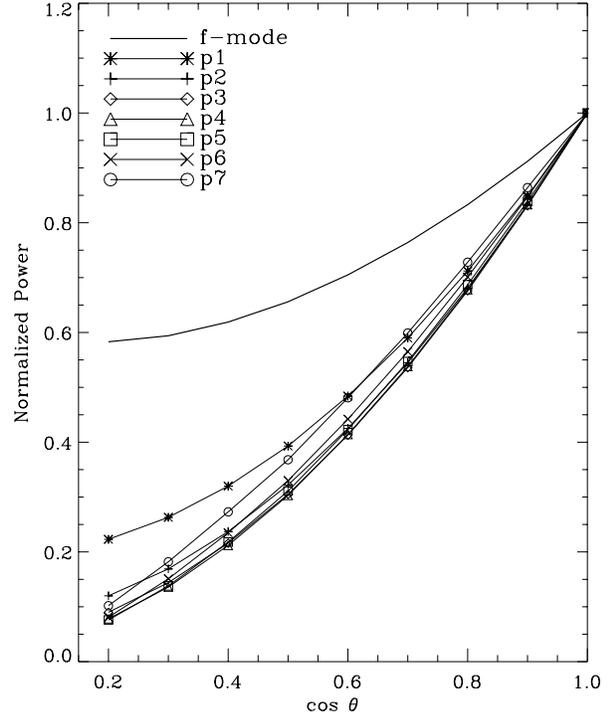

Fig. 9. Theoretical power distribution for $k_h = 0.5 \, \mathrm{Mm}^{-1}$

The second factor of (8) depends explicitly on γ. This factor causes an opposite trend in $\langle v_{\mathrm{los}}{}^2 \rangle$. Indeed this trend of decreasing line-of-sight amplitude always wins, except for the f mode very close to the limb.

For the two horizontal wave numbers $k_h = 0.5 \, \mathrm{Mm}^{-1}$ and $k_h = 1 \, \mathrm{Mm}^{-1}$, the centers of the two k_h ranges considered in the data analysis above, we have calculated the line-of-sight power as a function of the mode and position on the disk. For $k_h = 0.5 \, \mathrm{Mm}^{-1}$ the results are shown in Fig. 9; this figure must be compared to the observational results shown in Fig. 4b. There is qualitative agreement in that the power decrease towards the limb is weakest for the f mode, and that there is a reversal in the sequence of p modes at some intermediate mode number: At $\cos \theta = 0.5$, for example, the power (relative to disk center) has a minimum at p_2 in the observational result, and at p_4 in the theoretical model. The occurrence of such a minimum is a consequence of the combined effects of the inclination γ of the oscillation velocity vector and the dependence on height in the atmosphere. We conclude that both effects must be taken into account in an analysis of the center-to-limb variation of the wave spectrum, although a more detailed analysis might be necessary for a better agreement.

For the larger horizontal wave number $k_h = 1 \, \mathrm{Mm}^{-1}$ a similar comparison is more difficult. At this wave number there is almost no significant power in modes above p_4, which is the reason why these modes are not represented in Fig. 5. In addition, the theoretical model of evanescent waves in an isothermal atmosphere obviously is not applicable for modes with a frequency above the acoustic cut-off.

Generally, the observed velocity appears to be more vertical in the data than predicted by our simple model. Possible rea-

sons are plentiful: As far as the model is concerned, the real solar atmosphere is not isothermal, and the waves may behave in a non-adiabatic manner. For the determination of the dependence on height a detailed model for the center-to-limb variation of the Ni I 676.8-nm line profile may be required, possibly in combination with a velocity weighting function such as proposed by Beckers & Milkey (1975).

Schou & Bogart (1998), using MDI data obtained from May to July 1996, also investigated the contribution of the horizontal velocity component to the observed power at various positions on the disc. They found good agreement for the *difference* between the f and p_1 anisotropies with values expected from the approximation $|v_h/v_z| \simeq \omega_f^2/\omega^2$ (their Fig. 7, a and b, where ϕ corresponds to our θ); for the difference between p_1 and p_2 they suggest a similar agreement, but in this case their 'expected' result (the solid curves in their Fig. 7, c and d) appears to be too large by a factor of ≈ 2. Schou & Bogart conjecture that intrumental imperfections may lead to an imperfect point-spread function and so prevent the extraction of good absolute anisotropy values. This may in fact be another reason for the sometimes bad agreement between model and measurement in the present study. The difficulty may occur in particular near the limb, where the resolution becomes inferior, and in particular for the f mode with its rather small amplitude. In any case, for the *differences* between modes we obtain reasonable results, even for modes higher than p_2, – cf. Figs. 9 and 4b.

We finally remark that the present study confirms another result of Stix & Wöhl (1974): Horizontal sound waves, which appeared rather prominent in models that attributed the solar oscillations to local excitation by granules (Meyer & Schmidt 1967, Stix 1970), are absent. We find no power along the location of this mode, $\nu = ck_h/2\pi$, cf. the lower right corner of Fig. 2. This result seems interesting in view of the revival of modified local excitation models (Goode et al. 1992, Rimmele et al. 1995).

References

Beckers J.M., Milkey R.W., 1975, Solar Phys. 43, 289
Grossmann-Doerth U., 1994, A&A 285, 1012
Goode P.R., Gough D., Kosovichev A., 1992, ApJ 387, 707
Meyer F., Schmidt H.U., 1967, Z. Astrophys. 65, 274
Rimmele T.R., Goode P.R., Harold E., Stebbins R.T., 1995, ApJ 444, L119
Scherrer P.H., Bogart R.S., Bush R.I. et al., 1995, Solar Phys. 162, 129
Schou J., Bogart, R.S., 1998, ApJ 504, L31
Schröter E.H., 1985, Solar Phys. 100, 141
Stix M., 1970, A&A 4, 189
Stix M., 1989, *The Sun*, Springer, Berlin, Heidelberg
Stix M., Wöhl H., 1974, Solar Phys. 37, 63
Ulrich R.K., 1970, ApJ 162, 993
Vernazza J.E., Avrett E.H., Loeser, R., 1981, ApJS 45, 635